

3D SIMULATIONS OF RAYLEIGH-TAYLOR MIXING IN CORE-COLLAPSE SNE WITH CASTRO

C. C. JOGGERST,^{1,2} A. ALMGREN,³, S. E. WOOSLEY¹

Draft version June 4, 2018

ABSTRACT

We present multidimensional simulations of the post-explosion hydrodynamics in three different $15 M_{\odot}$ supernova models with zero, $10^{-4}Z_{\odot}$, and Z_{\odot} metallicities. We follow the growth of the Rayleigh-Taylor instability that mixes together the stellar layers in the wake of the explosion. Models are initialized with spherically symmetric explosions and perturbations are seeded by the grid. Calculations are performed in two-dimensional axisymmetric and three-dimensional Cartesian coordinates using the new Eulerian hydrodynamics code, CASTRO. We find as in previous work, that Rayleigh-Taylor perturbations initially grow faster in 3D than in 2D. As the Rayleigh-Taylor fingers interact with one another, mixing proceeds to a greater degree in 3D than in 2D, reducing the local Atwood number and slowing the growth rate of the instability in 3D relative to 2D. By the time mixing has stopped, the width of the mixed region is similar in 2D and 3D simulations provided the Rayleigh-Taylor fingers show significant interaction. Our results imply that 2D simulations of light curves and nucleosynthesis in supernovae (SNe) that die as red giants may capture the features of an initially spherically symmetric explosion in far less computational time than required by a full 3D simulation. However, capturing large departures from spherical symmetry requires a significantly perturbed explosion. Large scale asymmetries cannot develop through an inverse cascade of merging Rayleigh-Taylor structures; they must arise from asymmetries in the initial explosion.

Subject headings:

1. INTRODUCTION

Supernova 1987A has furnished astronomers with perhaps the best opportunity to study a core-collapse explosion to date. One of the most exciting discoveries to emerge from this event is the evidence for large-scale, extensive mixing in the supernova ejecta. γ -ray lines emitted by the decay of ^{56}Co were detected half a year earlier than expected for a spherically symmetric explosion model (Matz et al. 1988). Modeling the light curve in 1D requires a large amount of ^{56}Ni to be mixed outward and H and He to be mixed inward (Utrobin 2004). The Bochum event, in which fine-structure H α lines are observed 2 weeks after the explosion, is explained by the ejection of $10^{-3} M_{\odot}$ of ^{56}Ni moving with a velocity in excess of 4000 km s^{-1} into the far hemisphere of 1987A (Hanuschik et al. 1988). The Rayleigh-Taylor (RT) instability was posited as a possible explanation for the large-scale mixing implied for this explosion. Many groups using both SPH and grid-based codes simulated the evolution of 87A-like progenitor models, first in 2D, then in 3D. It soon became apparent that more than just the Rayleigh-Taylor instability is needed to explain the high ^{56}Ni velocities as well as the large degree of outward mixing of heavy elements and inward mixing of lighter elements. Simulations that posit modest initial perturbations are unable to replicate these features of the explosions. Kifonidis et al. (2006) find that by following the explosion from early times, and using large, low-order perturbations in the inner layers, they are able to replicate the high ^{56}Ni velocities and large

amounts of mixing seen in the explosion. The standing accretion shock instability (SASI) (Blondin et al. 2003; Blondin & Mezzacappa 2006; Scheck et al. 2006; Burrows et al. 2006, 2007; Marek & Janka 2009) provides a mechanism by which the inner parts of the ejecta could be deformed.

Most studies of the Rayleigh-Taylor instability in core collapse supernovae use 1987A-like progenitor models. However, supernovae in the high-redshift universe, as well as many modern day supernovae which die as red, not blue, giants, explode with presupernova structures which differ significantly from 1987A. This may greatly influence the evolution of the Rayleigh-Taylor instability in their outer layers. Simulations of rotating zero-metallicity supernovae (Ekström et al. 2008; Hirschi 2007) indicate that they may die as extended red, rather than compact blue, giants. Rotation mixes CNO elements to the base of the hydrogen-burning shell, where they catalyze the CNO cycle, greatly boosting the burning rate of H. This leads to the formation of a large convective envelope, effectively turning a compact blue star into a giant red one. Models indicate that the shell boost induced convection effectively mixes together the helium shell and the hydrogen envelope. The dense helium shell has been found to be important to the post-bounce evolution of 1987A-like progenitors (Hammer et al. 2009). Rotation has less of an effect on early stars with very low, but not zero, metallicity, such as the $Z = 10^{-4} Z_{\odot}$ progenitor models studied in Joggerst et al. (2010) as well as the current work. These stars remain blue. Solar metallicity stars end their lives as red giants, but retain their helium shells. Red stars should evolve differently from 1987A-type models after the supernova shock is launched. They are larger, so the shock takes longer to traverse the star, and the Rayleigh-Taylor instabilities have more time to develop (Chevalier 1976).

¹ Department of Astronomy and Astrophysics, University of California at Santa Cruz, Santa Cruz, CA 95060; cchurch@ucolick.org

² Theoretical Astrophysics (T-2), Los Alamos National Laboratory, Los Alamos, NM 87545

³ Computational Research Division, Lawrence Berkeley National Lab, Berkeley, CA 94720

Previous simulations of core-collapse explosions in two dimensions (Arnett et al. 1989; Hachisu et al. 1990; Fryxell et al. 1991; Herant & Benz 1991; Mueller et al. 1991; Herant & Benz 1992; Hachisu et al. 1992) have primarily focused on 87A-like progenitor models. Studies of Rayleigh-Taylor-induced mixing in three dimensions has exclusively focused on attempts to replicate observations of 1987A, and have found significant differences between simulations performed in two and three dimensions. The most successful of these 2D attempts, Kifonidis et al. (2003, 2006) found that to reproduce the high ^{56}Ni velocities observed in 1987A large initial asymmetries of low mode order were necessary. In studies of mixing in both red and blue supergiants (Joggerst et al. 2009; Herant & Woosley 1994) mixing is found to be more vigorous in red stars than in blue stars. Joggerst et al. (2010) evolve 36 models spanning three rotation rates, three explosion energies, three masses, and two metallicities in two dimensions, finding that mixing is more vigorous and goes on longer in stars that die as red as opposed to blue giants, in higher energy explosions, and in less massive stars. The literature on 3D simulations is more sparse. Kane et al. (2000) find that for a single-mode perturbation of 10% amplitude, Rayleigh-Taylor fingers grow 30 – 40% faster in 3D than in 2D. The most recent paper on the post-explosion hydrodynamics in 1987A (Hammer et al. 2009) use a successful explosion model from Scheck (2007) to initialize a 3D simulation, along with several 2D simulations derived from meridional slices through the initial explosion model. They find that for this model, which is highly asymmetric in the inner regions, the Rayleigh-Taylor instability grows faster and ballistically moving clumps of ^{56}Ni reach the hydrogen envelope in 3D. These clumps are effectively stopped by the dense He shell in the suite of 2D models initialized from slices through the Scheck (2007) model.

This is the first paper to simulate the post-explosion hydrodynamics of models with a diversity of presupernova structures in three dimensions. All models have the same mass ($15 M_{\odot}$) and explosion energy (1.2×10^{51} ergs at infinity), but two models explode as red giants and one as a more compact blue star. The red giant with zero metallicity effectively lacks a He shell because of convection arising from the hydrogen shell boost. The $Z = 10^{-4} Z_{\odot}$ and $Z = Z_{\odot}$ models both have helium shells, though the former is blue and the latter red at the time of explosion. This diversity of models allows us to see if presupernova structure has an impact on the subsequent evolution of nearly isotropic 2D as opposed to 3D models. These calculations set the stage for further study of asymmetric explosions in these diverse presupernova models.

The numerical methods employed in this study are discussed in Section § 2, and initial models and problem configuration are discussed in Section § 3. Results are presented in Section § 4, and are discussed and compared with previous 3D simulations in § 5. We offer some conclusions in § 6.

2. NUMERICAL ALGORITHMS

The multidimensional simulations described in this paper are performed with CASTRO (Almgren et al. 2010), an Eulerian adaptive mesh refinement (AMR) hydrodynamics code. Time integration of the hydrodynamics

equations in CASTRO is based on an unsplit higher-order piecewise parabolic method (PPM); the additional features are described below. All simulations described here used either axisymmetric coordinates in 2D or Cartesian coordinates in 3D.

2.1. Equation of State

We followed sixteen elements, from hydrogen through ^{56}Ni , so that our elemental abundances could later be used to compute spectra. The atomic weights and amounts of the elements are used to calculate the mean molecular weight of the gas required by the equation of state. The abundance of ^{56}Ni was followed separately in order to calculate the energy deposited by radioactive decay of ^{56}Ni and ^{56}Co .

The equation of state in our simulations is as described in Joggerst et al. (2010). It assumed complete ionization and included contributions from both radiation and ideal gas pressure:

$$P = f(\rho, T) \frac{1}{3} a T^4 + \frac{k_B T \rho}{m_p \mu} \quad (1)$$

$$E = f(\rho, T) \frac{a T^4}{\rho} + 1.5 \frac{k_B T}{m_p \mu}, \quad (2)$$

where P is the pressure, a is the radiation constant, k_B is Boltzmann's constant, T is the temperature, ρ is the density, m_p is the proton mass, μ is the mean molecular weight, and E is the energy.

The function $f(\rho, T)$ is a measure of the contribution of radiation pressure to the equation of state that accounts for the fact that radiation ceases to be trapped at some point. It is 1 in regions where radiation pressure is important, i. e. where gas is optically thick, and 0 in regions where radiation pressure is unimportant, i. e. where gas is optically thin, with a smooth transition in between. The function $f(\rho, T)$ takes the form

$$f(\rho, T) = \begin{cases} 0 & \text{if } \rho \geq 10^{-9} \text{ gm cm}^3 \\ & \text{or } T \leq T_{neg} \\ f(T) = e^{-\frac{T_{neg}-T}{T_{neg}}} & \text{if } \rho < 10^{-9} \text{ gm cm}^3 \\ & \text{and } T > T_{neg} \end{cases}$$

where T_{neg} is the temperature at which contributions to the pressure from radiation are 100 times less than that contributed by ideal gas pressure:

$$T_{neg} = \frac{3k_b \rho}{100 m_p \mu a}^{1/3}. \quad (3)$$

Radiation pressure will begin to dominate the equation of state above T_{neg} without some adjustment, even though this is unphysical, as radiation pressure is negligible in optically thin regions. Damping the radiation component of the EOS with the function $f(\rho, T)$ in these regions provides a more physical solution.

2.2. Radioactive Decay of ^{56}Ni

Energy from the radioactive decay of ^{56}Ni to ^{56}Fe was deposited locally at each mesh point, in the same manner as described in Joggerst et al. (2010). The rate at which energy from the decay of ^{56}Ni to ^{56}Co was deposited in the grid is given by:

$$dE_{Ni} = \lambda_{Ni} X_{Ni} e^{-\lambda_{Ni} t} q(Ni). \quad (4)$$

The decay rate of ^{56}Ni , λ_{Ni} , is $1.315 \times 10^{-6} \text{ s}^{-1}$, and the amount of energy released per gram of decaying ^{56}Ni is $q(Ni)$, which we set to $2.96 \times 10^{16} \text{ erg g}^{-1}$. X_{Ni} is the mass fraction of ^{56}Ni in the cell. The mass fraction of ^{56}Co at a given time can be expressed in terms of the mass fraction of initial ^{56}Ni by

$$X_{Co} = \frac{\lambda_{Ni}}{\lambda_{Co} - \lambda_{Ni}} X_{Ni} (e^{-\lambda_{Ni}t} - e^{-\lambda_{Co}t}), \quad (5)$$

so that the energy deposition rate from ^{56}Co is

$$dE_{\phi} = \frac{\lambda_{Ni}}{\lambda_{Co} - \lambda_{Ni}} X_{Ni} (e^{-\lambda_{Ni}t} - e^{-\lambda_{Co}t}) \lambda_{Co} q(Co). \quad (6)$$

We assumed a decay rate $\lambda_{Co} = 1.042 \times 10^{-7} \text{ s}^{-1}$ and an energy per gram of decaying ^{56}Co , $q(Co)$, equal to $6.4 \times 10^{16} \text{ erg g}^{-1}$.

2.3. Gravity

Although **CASTRO** supports several different approaches to solving for self-gravity, we used the monopole approximation for gravity in the calculations presented here, as discussed in Joggerst et al. (2010). Because the density profiles in the simulations depart very little from spherical symmetry, the gravitational field constructed using the monopole approximation is nearly identical to that found by solving the full Poisson equation for the gravitational potential, and using the monopole approximation significantly reduces the computational cost of the calculations.

Gravity from a point mass located at the origin was also included in the gravitational potential. The point mass represents the compact remnant left behind by the SN explosion. As infalling matter crosses the zero-gradient inner boundary near the origin, it is added to this point mass.

2.4. Adaptive Mesh Refinement

CASTRO's AMR algorithm uses a nested hierarchy of logically-rectangular grids with simultaneous refinement of the grids in both space and time. The integration algorithm proceeds recursively, advancing coarse grids in time, then advancing fine grids multiple steps to reach the same time as the coarse grid, and finally synchronizing the data at different levels.

The regions of refinement evolve throughout the simulation based on user-specified refinement criteria applied to the solution. In the simulations presented here, re-gridding of all grids at level $\ell + 1$ and above occurred every two level ℓ time steps.

Our refinement criteria are based on the ‘‘error estimator’’ of Löhner (1987), which is essentially the ratio of the second derivative to the first derivative at the point at which the error is evaluated. Details of the implementation are discussed more fully in Almgren et al. (2010). The result is a dimensionless, bounded estimator, which allows arbitrary variables to be subjected to the same criterion for error estimation. In these calculations, density, pressure, velocity, and the abundances of ^{56}Ni , He, and O were used as refinement variables, with the elemental abundances only used in a particular region if their abundance was greater than 10^{-3} .

3. SIMULATIONS SETUP AND EXECUTION

The simulations presented here were carried out in two distinct stages. First each stellar model was evolved in one dimension using the code **KEPLER** to the point where the core became unstable to collapse. It was then artificially exploded by means of a piston located at the base of the oxygen shell with enough energy that the explosions had 1.2×10^{51} ergs of energy at infinity. The models were evolved forward in one dimension for 20 seconds for models z15 and u15, and 100 seconds for s15, until all nuclear burning had ceased.

These profiles were then mapped onto a two-dimensional r-z or three-dimensional Cartesian grid in **CASTRO**, and the calculation was evolved until the shock reached the edge of the simulation domain. The calculation was then stopped, the domain enlarged, and the calculation restarted within the larger domain (see § 3.3 below). Data to fill the new regions of the enlarged domain were supplied from the same one-dimensional profile that was used to initialize the multidimensional calculation.

This process continued until the models had evolved out to radii where Rayleigh-Taylor mixing ceased and the star was expanding essentially homologously. We computed three $15 M_{\odot}$ models, at zero, $10^{-4} Z_{\odot}$, and solar metallicities.

3.1. Progenitor Models

Three different supernova models, representing three different metallicities, are presented in this paper. Model z15 has zero initial metallicity, and represents a Population III (Pop III) star. Model u15 has $Z = 10^{-4} Z_{\odot}$, and model s15 has solar metallicity. All models are derived from rotating $15 M_{\odot}$ progenitors. The zero and low metallicity models presented in this paper are the same as presented in Joggerst et al. (2010) and Zhang et al. (2008). The solar metallicity model, model s15, is similar to the model presented in Woosley & Heger (2007). For moderate values of rotation, the amount of rotation was found to have little effect on its post-explosion evolution (Joggerst et al. 2010). There are, however, profound differences between rotating and non-rotating zero metallicity supernovae. Several studies (Ekström et al. 2008; Hirschi 2007; Joggerst et al. 2010) have found that a small amount of rotation in zero metallicity massive stars dredges up enough carbon, nitrogen, and oxygen from the helium burning shell to catalyze a CNO cycle at the base of the hydrogen envelope. This leads to rapid burning and a shell boost that triggers convection, mixing most of the helium and hydrogen shells together, and ‘‘puffing up’’ the outer envelope of the star. This is apparent in Figure 1. Models with a small amount of metals (i. e. u15 in this paper) do not show this shell boost behavior, and die as blue supergiants. Rotation also has little effect on the presupernova structure of the solar metallicity model s15, which dies as a red giant.

3.2. Initialization of Multidimensional Data

In mapping the radial data from **KEPLER** onto the multidimensional grids in **CASTRO**, special care was taken to properly resolve the key elements of the simulations: the shock, the elemental shells, and the ^{56}Ni at the center of the explosion. In particular, both the ^{56}Ni and the O shell were resolved with a minimum of 16 cells at

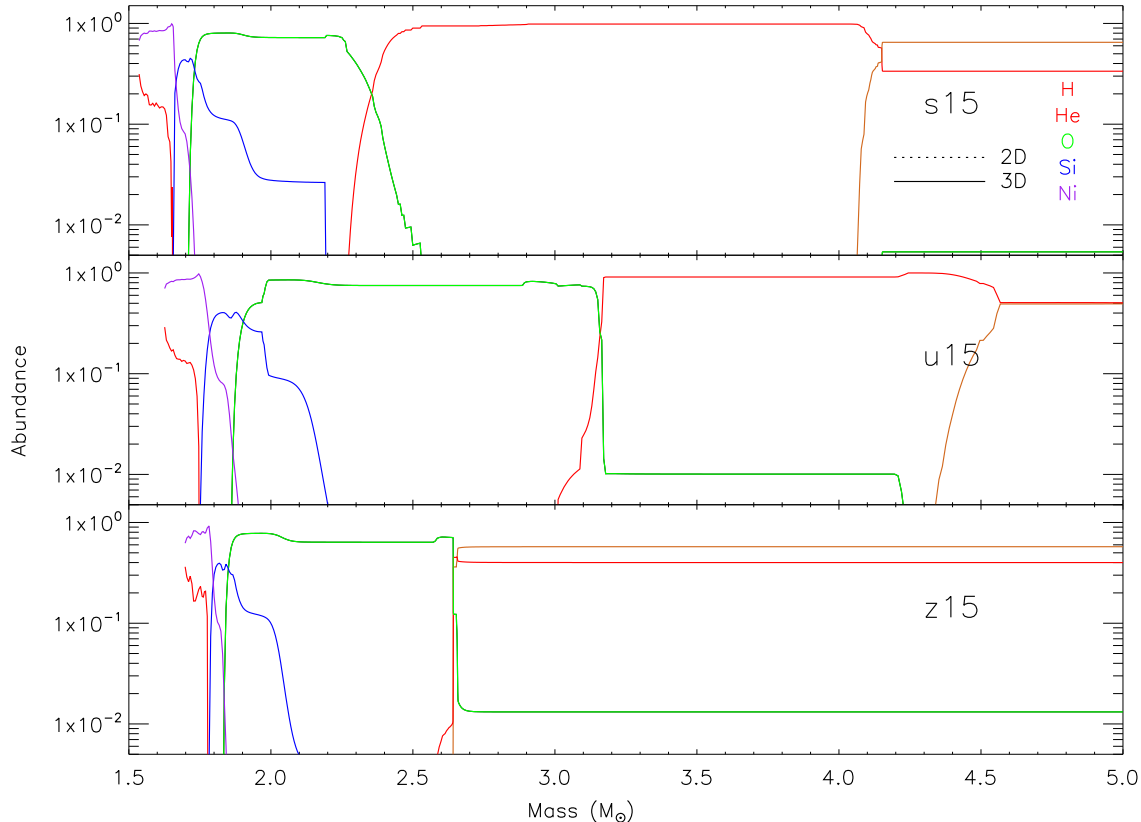


FIG. 1.— Shell structure for H, He, O, Si, and Ni for our initial models. Other elements were included in our simulations but are left out of the figure for clarity. Note that while s15 and u15 (top and middle figures) show an He shell, this shell is not present in model z15 because of convection arising from a hydrogen shell boost. The models are 15 solar masses, but the outer layers are essentially a continuation of the levels at the right hand side of the plot, and have been omitted to better show the detail in the center.

the highest level of refinement. This mapping results in explosions that are spherically symmetric in **CASTRO**; low-order departures from spherical symmetry are suppressed. Our models therefore only capture higher-order asymmetries in the explosions.

Perturbations that give rise to the Rayleigh-Taylor instabilities are seeded from the axisymmetric or Cartesian grid. We performed calculations in 2D at twice the resolution of the simulations considered in this paper and compared the results of the high resolution simulations to the low resolution simulations. The width of the mixed region and velocities of the elements were essentially the same, indicating that our results are numerically converged and do not depend on the initial scale of perturbations imposed by the grid.

3.3. Enlarging the Domain

In order to minimize the amount of computational resources used, we implemented a strategy of enlarging the simulation domain only as necessary as the size of the region of interest increased in time. The simulations were initialized on a 128^n grid with 2 levels of refinement, where n is the dimensionality of the simulation. This gives an effective grid resolution of 512^n at the finest level. A given simulation was advanced in time to the point where the shock was near the edge of the domain. The simulation was then stopped and the domain was doubled in each coordinate dimension. The enlarged domain was covered by grids with cell spacing twice that

of the previous coarsest resolution, so that after each enlargement the base grid continued to be 128^n . The simulation then had 3 levels of refinement; in most cases (except for u15) the highest level of refinement was removed at this point, reducing the finest resolution by a factor of 2 as well. This allowed us to tailor the size of the domain to the size of the region of interest, without wasting computational resources in regions where nothing of interest was happening. Each time the domain was enlarged data from the new regions of the domain were interpolated from the original model.

To ensure that the strategy described above did not affect the results of the simulations relative to analogous calculations performed on domains which were larger throughout, we ran two-dimensional simulations in which the final domain size was imposed from the start. The results were essentially the same, although more complex mixing structures are visible in the case with the initially larger domain. The width of the mixed region remains the same, i.e. heavy elements are mixed out the the same point in radius and mass, while lighter elements are mixed inward to the same point in the both cases. The velocities obtained by the elements are the same. This is sufficient evidence that the strategy of enlarging the domain throughout the calculation did not introduce spurious artifacts.

4. RESULTS

In each multidimensional simulation presented here, when the shock encountered the large region of increas-

ing ρr^3 at the base of the hydrogen envelope of the presupernova star (or, in the case of model z15, the helium-hydrogen envelope) it slowed, giving rise to a reverse shock. The reverse shock then propagated inwards in mass towards the center of the star, and left a reversed pressure gradient in its wake. This triggered the Rayleigh-Taylor instability first between the helium shell and the hydrogen envelope, and then between the helium and oxygen layers of the supernova. For model z15, this instability first arose between the oxygen layer and the helium-hydrogen envelope. The instability grew, mixing together layers of increasing atomic mass as the reverse shock propagated inward through the star. Eventually the reverse shock passed by, and mixing stopped once the Rayleigh-Taylor fingers had dissipated their momenta.

In each simulation, the domain was enlarged five times, bringing the final effective resolution of each simulation to $16,384^n$, where n is the dimensionality of the simulation. For model u15, four levels of refinement were retained at the final stage of the simulation; for models s15 and z15, two levels of refinement were retained.

Mixing had effectively ceased by 4.0×10^5 seconds for model s15, 3.8×10^4 seconds for model u15, and 1.7×10^5 seconds for model z15. Mixing had stopped by similar times in 2D and 3D simulations. The models were run to twice this time to make sure that no additional mixing would occur.

Shown in Figure 2 are snapshots at identical times for the two- and three-dimensional simulations of models (from top) s15, u15, and z15. The abundance of He, O, Si, and ^{56}Ni are shown in a logarithmic scale, starting clockwise from top left. These snapshots correspond to times when mixing had effectively stopped in the different models. On the left are snapshots of the 2D models; at right are snapshots showing slices in the YZ plane at the X axis. Upon first inspection, there appears to be very little difference between the two and three dimensional simulations of all three models. The width of the mixed region appears the same between the 2D and 3D models, although mixing in the 3D models appears to be more complete in this region than in the 2D models. The shape of the instability differs slightly between the 2D and 3D simulations. The mushroom shape of the instability is more clearly defined in 2D than in 3D, especially for model u15, where the instability had less time to grow and thus retained its original shape more clearly. In the 3D models, the Rayleigh-Taylor instability appears more elongated, in line with what was found in the single mode study of Kane et al. (2000). The greatest difference between the 2D and 3D simulations arises in model s15, shown at the bottom of Figure 2, where there is actually *less* mixing of ^{56}Ni in 2D than in 3D.

In all models the Rayleigh-Taylor fingers have grown to the point where they have begun to interact with one another. Models z15 and s15, in which the RT instability had the longest time to grow, show the greatest degree of interaction. This interaction transfers energy and momentum in the transverse directions to the blast wave, leading to a transition to turbulence in 3D, and to a chaotic regime in 2D (Remington et al. 2006). Miles et al. (2005) state that this transition to turbulence begins to happen when the Rayleigh-Taylor fingers are about 5 to 6 times longer than their initial wavelength. This has clearly happened in all simulations. Models z15

and s15 appear strikingly similar to the fully turbulent simulations presented in Miles et al. (2005).

The differences between 2D and 3D can be compared more quantitatively by examining Figure 3. This figure displays the radial average of abundances for significant elements in both 2D and 3D simulations of the three models after all mixing has stopped. The times shown are the same times as in Figure 2. Figure 3 shows clearly that the width of the mixing region in the 2D and 3D models is nearly the same. ^{56}Ni is the exception, and is slightly more mixed in 2D than in 3D in the simulations of model s15. Previous simulations of the Rayleigh-Taylor instability in which these fingers do not interact show $\approx 30\%$ faster growth rate in 3D than in 2D, resulting in a wider mixed region in 3D. We also see a faster initial growth rate in 3D than in 2D, but once the Rayleigh-Taylor fingers begin to interact with one another, the growth rate in the 3D models decreases and the final width of the mixed region is the same between 2D and 3D. This is in line with simulations of the Rayleigh-Taylor instability in a laboratory context presented in Miles et al. (2005), in which the RT fingers interacted.

The 2D and 3D simulations do appear somewhat different in Figure 3 in that the 3D lines are smoother than the 2D lines. Because interactions between Rayleigh-Taylor fingers can transfer momentum and energy perpendicular to the direction of the blast wave, mixing proceeds to a greater extent in 3D than in 2D. This reflects the fact that the 3D simulations have become fully turbulent (in the case of z15 and s15), while the 2D simulations are chaotic, as 3D simulations are able to transfer momentum and energy in two dimensions transverse to the blast wave, while 2D simulations have only one transverse dimension at their disposal. There is likely a sampling effect at play here, as well. In 2D, there simply are not as many Rayleigh-Taylor fingers as there are in 3D, and thus there is effectively a smaller sample of the instabilities that grow. In 3D there are more Rayleigh-Taylor structures, so the space the fingers can occupy is better sampled, leading to a smoother radialized distribution.

The velocities obtained when mixing has effectively ceased are virtually identical between the 2D and 3D simulations, as shown in Figure 4. These simulations are shown at different times: 4.0×10^5 seconds, 3.8×10^4 seconds, and 1.7×10^5 seconds for models s15, u15, and z15, respectively, and so direct comparison of one model with another would be misleading, as the material will slow down as time goes on. It is clear from Figure 4 that the ultimate velocities after mixing has stopped and the Rayleigh-Taylor instability has frozen out are essentially the same in the 2D and 3D simulations. This is different from what Hammer et al. (2009) found in their simulations with larger degrees of initial asymmetry. They saw a high velocity tail for ^{56}Ni , O, and Si. We do not see a high velocity tail here.

The 3D renderings shown in Figure 5 give a clearer picture of the shape of the Rayleigh-Taylor instabilities in our simulations than the slice through the 3D plane shown in Figure 2. We show renderings of the outermost surfaces of carbon, oxygen, silicon, and nickel. Model s15 is shown at the left, model u15 in the center, and model z15 at the right. These renderings were taken at different times, but after mixing had frozen out. Only in model z15 have bits of the oxygen shell broken off and begun to

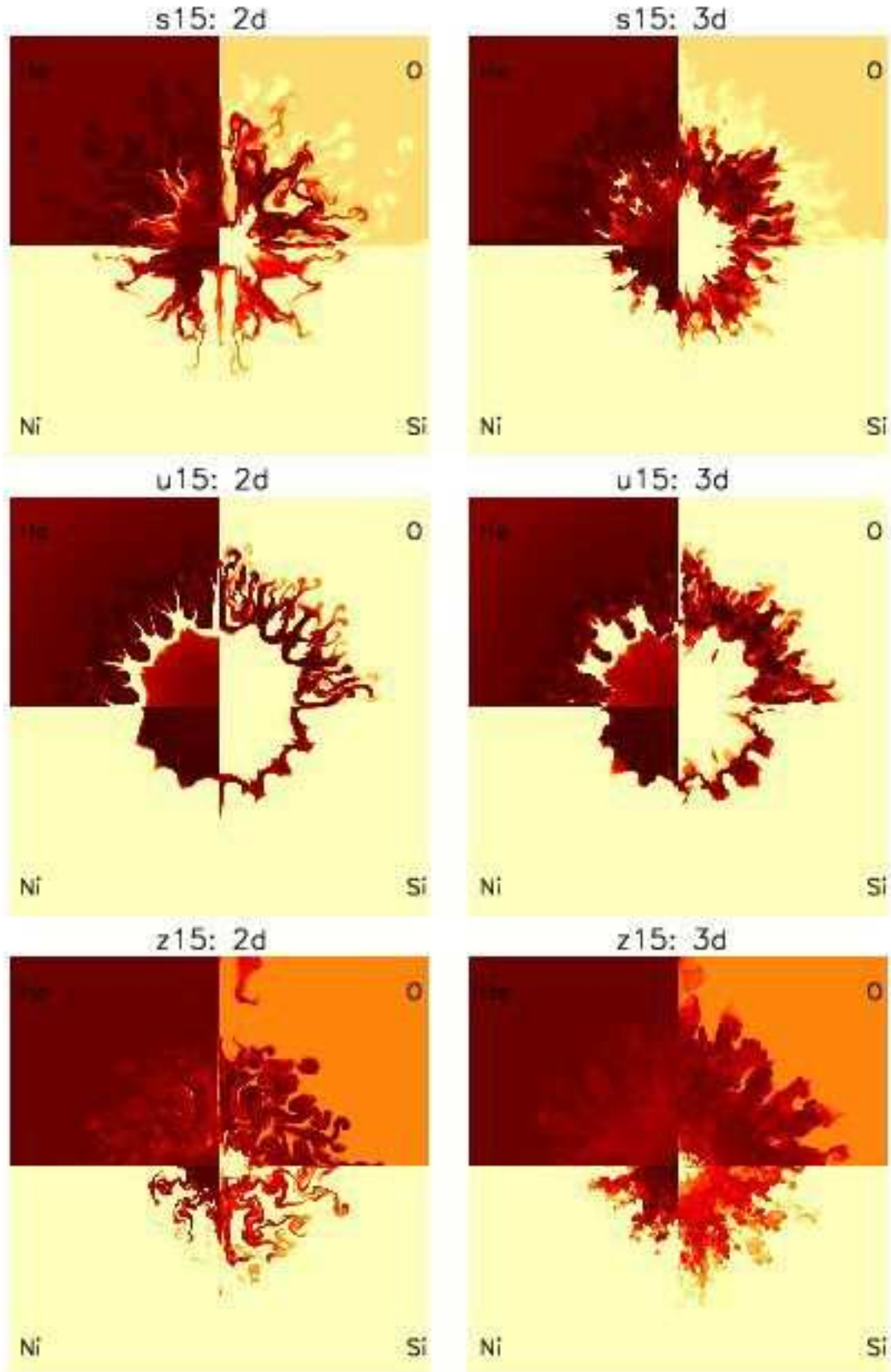


FIG. 2.— Snapshots of elemental abundance in the 2D (left) and 3D (right) versions of (from top to bottom) models s15, u15, and z15. The 3D snapshots are slices at the X axis through the YZ plane. Because of artifacts in CASTRO, the extent of mixing is likely to be slightly exaggerated in slices at an axis. Nevertheless, the width of the mixed region in 2D and 3D appear very similar in all models. There is even slightly less mixing of ^{56}Ni in model s15 in 3D than in 2D. The shape of the instability differs slightly between 2d and 3d in the expected manner—the 2D shapes are slightly more “mushroomed” and the 3D shapes are more elongated, with the 3D models appearing to have transitioned to a fully turbulent regime, but otherwise the two simulations appear very similar.

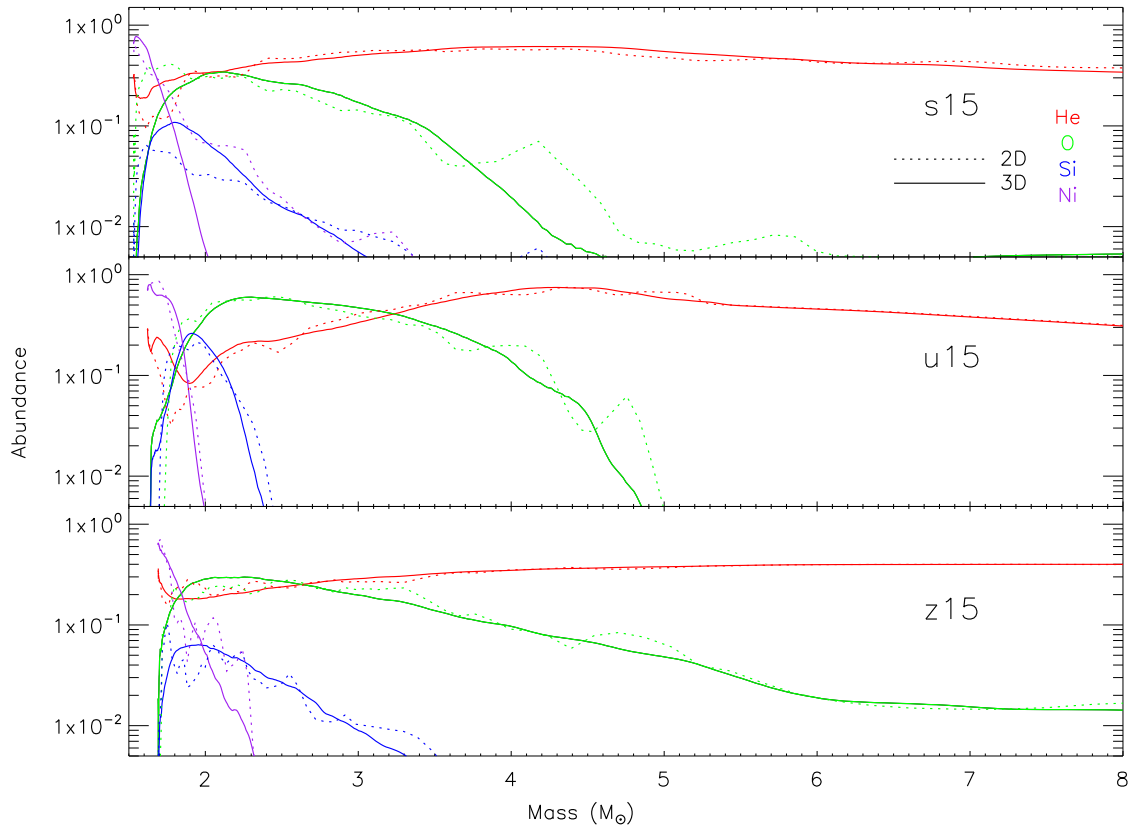


FIG. 3.— Abundance by mass of individual elements as a function of mass coordinate. The width of the mixed region is essentially the same between the 2D and 3D cases, though 3D is smoother. The higher mass coordinate layers of the simulations have been omitted from the plot to better show the details of their inner portions.

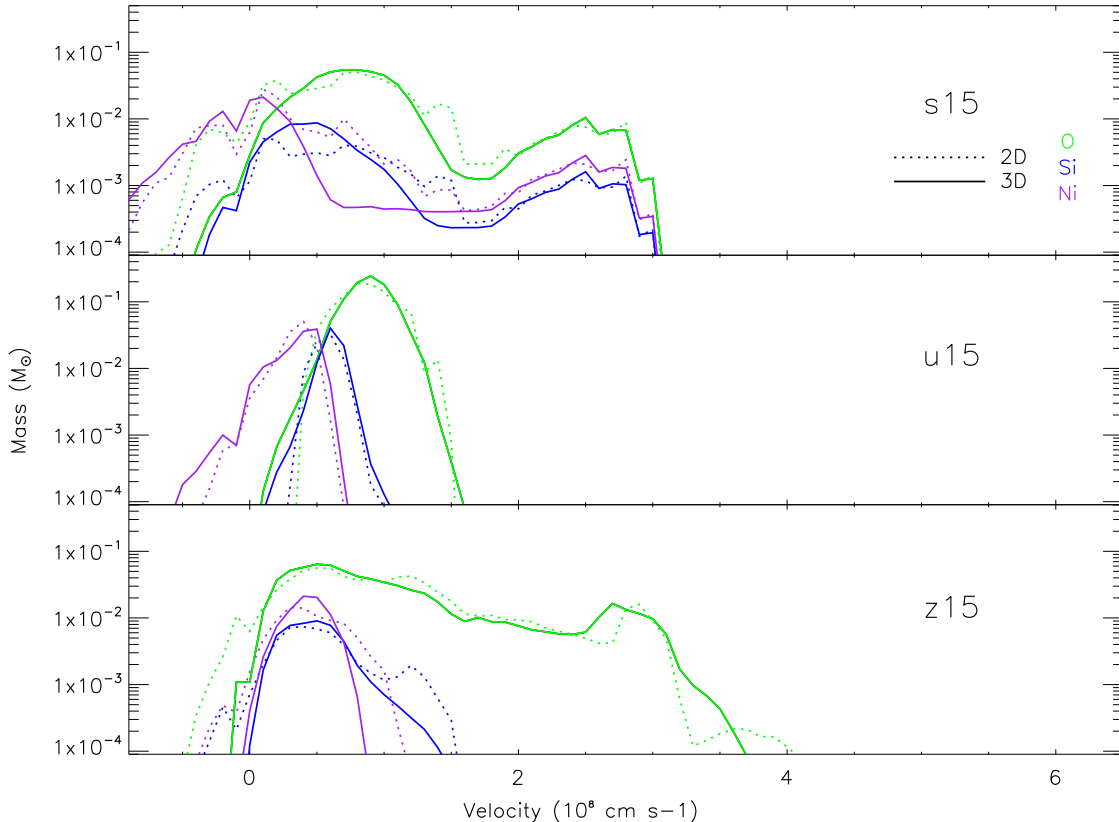


FIG. 4.— Mass of individual elements as a function of velocity per 100 km s^{-1} velocity bin. The amount of heavier elements such as O and ^{56}Ni at high velocities is essentially the same in 2D and 3D. Where the two differ, as they do most significantly for Ni and Si in models s15 and z15, the 2D simulations actually show material mixed out to higher velocities than the 3D simulations.

move through the H-He shell that surrounds the heavy element core of this star. For no models have clumps of heavier elements penetrated shells of lighter elements, as happened in the asymmetric explosion modeled by Hammer et al. (2009). Even the broken-off clumps of oxygen visible in the right hand panel of Figure 5 are encased in a layer of carbon. It is also apparent by examining this figure that mixing has progressed further in the simulations where the progenitor star was a red giant, model s15 and z15, than for model u15, whose progenitor died as a more compact blue star. The original shape of the instability can be seen in the carbon surface (top middle panel). In addition, the ^{56}Ni at the center of the model is less deformed in this model than in previous models. The most vigorous mixing has taken place in model z15, which lacked a dense helium shell and died as a red giant.

5. DISCUSSION

Previous simulations of the Rayleigh-Taylor instability in core collapse supernovae have found significant differences between similar calculations performed in two and three dimensions. Kane et al. (2000) examined the growth of Rayleigh-Taylor fingers arising from a single mode perturbation, and found that the instability grew 30 – 35% faster in 3D than in 2D in a 1987A-type progenitor model. This faster growth rate was not sufficient to replicate observations of 1987A, however. In the more recent paper of Hammer et al. (2009), the authors performed simulations of a 1987A-type model in two and

three dimensions, starting with a more realistic initial model from Scheck (2007). Their initial model was in the first stages of the explosion, and showed large-scale asymmetry in the heavy element core. They found, again, that single perturbations grew around 30% faster in 3D than in 2D. The authors proposed that artificial drag forces arising from 2D geometry slow down the growth of the instability in 2D simulations relative to 3D simulations, where these artificial drag forces are not present. This was also described in Kane et al. (2000), who explain that the rising bubbles have less effective matter to push out of the way in 3D than in 2D.

The Hammer et al. (2009) study also found that in 2D, rising bubbles of heavy elements became entrained in the dense He shell left behind by the shock. In 3D, however, these bubbles were able to burst through the He shell to reach the H envelope, replicating one of the key observations of 1987A.

Studies of the Rayleigh-Taylor instability outside the context of supernova explosions have also found that a single Rayleigh-Taylor instability grows about 30% faster in 3D than in 2D (Anuchina et al. 2004). Previous simulations of the Rayleigh-Taylor instability in a laboratory context (Miles et al. 2005) have found that the width of the mixed region is very similar between 3D and 2D, provided that the individual Rayleigh-Taylor fingers interact. Initially, the Rayleigh-Taylor fingers grow faster in 3D than in 2D. Once the fingers begin to interact, 3D simulations transition to turbulence more completely than 2D simulations. 3D simulations can transfer mo-

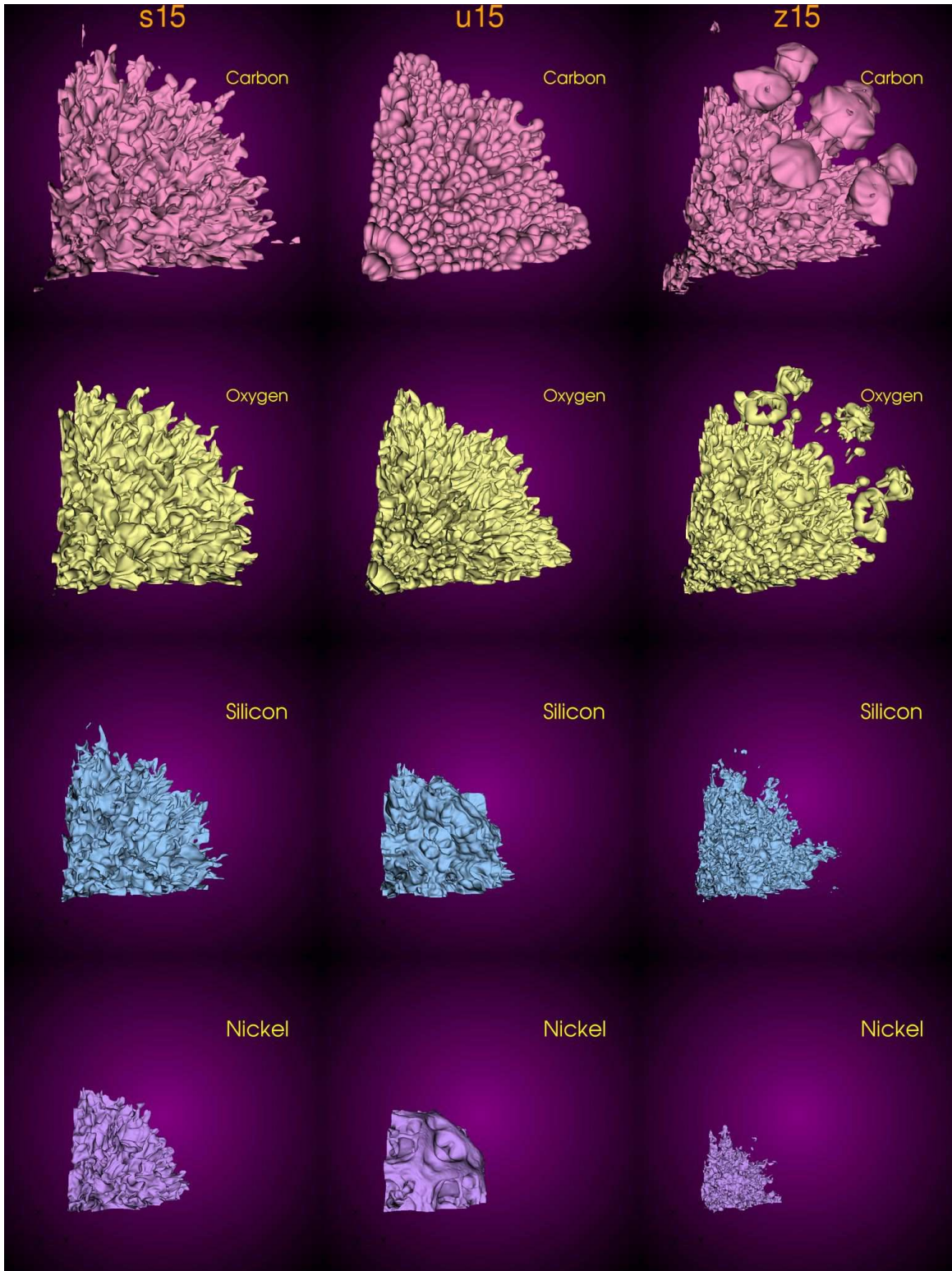


FIG. 5.— 3D renderings of the outermost surface of carbon, oxygen, silicon, and nickel after mixing has frozen out. At left is model s15; center is u15, and right is z15. Note that while the scale and time are consistent within models, the 3 models are shown at different scales and time: 5×10^{13} cm and 4.0×10^5 seconds for s15, 5×10^{12} cm and 3.8×10^4 seconds for model u15, and 3×10^{13} cm and 1.7×10^5 seconds for model z15. For no model did heavier, inner layers penetrate the lighter, outer layers, though for model z15 clumps of material have broken off and moved a small distance into the H-He envelope.

mentum in two dimensions perpendicular to the blast wave, while 2D simulations can transfer momentum in only one transverse direction. This results in more complete mixing within the mixed region in 3D than in 2D, reducing the Atwood number in 3D relative to 2D.

For the simplest case of two incompressible fluids under constant acceleration with an initial perturbation of wavelength λ and amplitude η , such that $\eta \ll \lambda$, the growth rate of the instability is given by Rayleigh (1883):

$$\frac{d\eta}{dt} = \left(\frac{2\pi Ag}{\lambda} \right)^{1/2} t \quad (7)$$

where g is a constant acceleration and t is time. A , the Atwood number, is defined by

$$A \equiv \frac{(\rho_2 - \rho_1)}{(\rho_2 + \rho_1)} \quad (8)$$

where ρ_1 and ρ_2 are the densities of the light and heavy fluids, respectively.

As the densities of the two fluids become comparable, the Atwood number becomes smaller and the growth rate decreases. The growth rate of the bubbles in 3D is thus reduced, neatly canceling out the reduced drag these same bubbles experience in 3D as opposed to 2D. The width of the mixed region remains essentially the same between 2D and 3D for cases where the Rayleigh-Taylor fingers interact with one another.

It could be supposed that the reason the final state of the supernova remnant appears the same in our 2D and 3D models is that the perturbations arising from the grid were somehow larger in 2D than in 3D, and this effect exactly cancelled out the faster growth rates we expect to see in 3D. But this is not the case. Perturbations arising from the grid are larger in 3D than in 2D. These perturbations arise because we try to fabricate a spherical object with boxes, as required by the RZ and Cartesian geometries used in our simulations. The maximum amount one would expect to depart from a sphere (or circle) in space is equivalent to the longest distance across a single cell, which in 2D is $\sqrt{2}\Delta x$ and in 3D is $\sqrt{3}\Delta x$. To make certain, we performed the same set of calculations in 2D at twice the resolution. These simulations give the same results as our less refined simulations, indicating that our simulations are numerically converged for the problem presented here.

As in the simulations of Miles et al. (2005), Kane et al. (2000), and Hammer et al. (2009), we find that the Rayleigh-Taylor instability initially grows faster in 3D than in 2D. As the Rayleigh-Taylor fingers grow to the point where they begin to interact with one another the simulations begin to transition to a turbulent (3D) or chaotic (2D) regime. In 3D, momentum is transferred from the fingers in two dimensions, as opposed to only one dimension in 2D. The transition to turbulence in 3D results in more complete mixing within the mixing region than the 2D simulation, reducing the Atwood number in 3D relative to 2D. This has the effect of reducing the growth rate of the instability in 3D relative to 2D. The reduced growth rate in 3D relative to 2D at late times compensates for the fact that the bubbles do indeed experience less drag in 3D than in 2D, and grow faster at early times. By the time mixing has ceased, the width

of the mixed region is nearly identical in 2D and 3D in models where the Rayleigh-Taylor fingers have time to interact with one another.

It can be seen from Eq. 7 that instabilities seeded by long wavelength perturbations grow more slowly than those seeded by short wavelength perturbations. Obviously, the interior of a supernova deviates from the ideal case: the acceleration is not constant, the fluids are compressible, and η soon becomes of the same order as λ . In order for long wavelength perturbations to dominate before mixing ceases there must be significant initial power at long wavelengths. Because there is less time for the instability to grow in blue stars, we expect to see more traces of large perturbations at fairly low wavenumbers in these stars than in red stars. The simulations of Hammer et al. (2009) have a significant amount of power at long wavelengths, so these perturbations grow fast enough to dominate before mixing is truncated.

The initial perturbations in our simulations are a great deal smaller than those examined in previous studies. The spectrum of these perturbations is also flatter and made up of higher modes. The perturbations are more random, though, it should be noted, not entirely so, and are largest around the 30 and 60° marks on the grid. This can be seen during the initial stages of the development of the instability, though not at later times, for model s15. The enhanced perturbations at these points is likely behind the placement of the clumps visible in the 3D rendering of model z15 in Figure 5.

Mixing had more time to develop in our two red giant stars, models z15 and s15, than it generally does in the blue giant 1987A-type progenitor models studied in Kane et al. (2000) and Hammer et al. (2009). Mixing froze out after $4x10^5$ and $1.7x10^5$ seconds for the red models s15 and z15, respectively, over an order of magnitude later than in the simulation of Hammer et al. (2009), in which mixing froze out after $9x10^3$ seconds. In our blue u15 model, mixing froze out after $4x10^4$ seconds, which is still nearly 5 times longer than in the Hammer et al. (2009) model. The individual Rayleigh-Taylor instabilities in all simulations grew for sufficient times that they interacted, though more interaction took place in the red models. This was not the case in the single-mode perturbation explored in Kane et al. (2000), or the few large perturbation modes in (Hammer et al. 2009). Smaller wavelengths grow faster than longer wavelengths, so longer wavelength perturbations are less likely to become nonlinear. In these models, as well as the single instability investigated in Anuchina et al. (2004), the Rayleigh-Taylor fingers did not interact with one another, ensuring that the relative drag on the fingers was the only significant difference between 2D and 3D. This accounts for the around 30% faster growth rates discovered in these simulations. The simplicity of the initial perturbation spectrum can delay the transition to turbulence, and hence make mixing appear more efficient in 3D than in 2D (Miles et al. 2005).

For long enough wavelength perturbations, spherical geometry will ensure that the perturbations diverge, so they never interact and thus never enter a turbulent regime. This will quickly lead to significant departures from axisymmetry. There may exist a transition mode perturbation which would be the longest wave-

length mode that could lead to turbulent interaction. The instabilities will diverge without interaction if the wavelength of an instability is greater than the height at which it would become nonlinear. This transition mode ought to be dependent on presupernova structure: red supergiants have longer time for the Rayleigh-Taylor instability to grow, and thus potentially a lower mode than blue giants.

The Rayleigh-Taylor instability may “forget” its initial conditions at late times. This can happen though an inverse cascade, where shorter wavelength bubbles merge to form longer wavelength structures. Under idealized conditions, the flow may become self similar. This transition to self-similarity likely happens during the early stages of Rayleigh-Taylor growth in our simulations, accounting for the similar end appearance of our simulations despite increasing the resolution (and decreasing the initial perturbations). This inverse cascade can only lead to the instabilities becoming so big. A necessary condition for self-similarity is that

$$\lambda \ll h \ll L \quad (9)$$

where h is the height of the instability and L is the size of the region in which the instability is growing. The merger of short wavelength instabilities to larger wavelength instabilities should be truncated long before λ becomes comparable to L , which would produce large-scale asymmetries. Large-scale departures from symmetry must arise from the supernova explosion mechanism itself, as they cannot arise through an inverse cascade of the Rayleigh-Taylor instability.

Recent observations suggest that asymmetry in core-collapse type supernova explosions is common (Wang & Wheeler 2008). For SNe type II, this asymmetry is characterized by a dominant polarization angle, which is most likely due to a directed, jet-like flow. Polarization data show that most SNe also exhibit composition-dependent, large scale departures from axisymmetry. The degree of departure from axisymmetry may be less in SNeII-P; Chugai et al. (2005) and Chugai (2006) are able to match observations of one SNeII-P, SN2004dj, by using a bipolar distribution of ^{56}Ni . This fits with the emerging picture of collapse supernova mechanisms, which are likely to be inherently multidimensional and aspherical (Janka et al. 2007) The SASI explosion mechanism (Burrows et al. 2006; Scheck et al. 2006; Marek & Janka 2009) seems to be one of the better candidates for reviving the stalled shock and successfully exploding a massive star, and it is inherently asymmetric. How relevant, then, are spherical explosion models? This is the first time the post-explosion hydrodynamics of a wide range of supernova progenitors has been studied in 3D. It is reasonable to model Pop III and Pop II core collapse SNe in 3D first as spherical explosions as no observations of these primordial supernovae have yet been made. This study will contextualize future studies of supernovae progenitors with asymmetric explosions.

For type II SNe in which departures from asymmetry are small and dominated by an axisymmetric component, 2D simulations may do as well as 3D simulations in reproducing the axisymmetric features of the supernova remnant. In these stars, Rayleigh-Taylor fingers of all but the lowest mode order are expected to grow far enough

that they begin to interact with one another. Simulations in 2D of such stars can be used to predict nucleosynthesis and fallback for such explosions with a fair degree of accuracy, as was done in Joggerst et al. (2010). 2D calculations may also be used to more accurately predict light curves of SNe for which departures from axisymmetry do not dominate, which would use far less computational resources than similar calculations performed in 3D.

6. CONCLUSIONS

We have performed two and three dimensional simulations of supernova models with three different metallicities: model z15, with $Z = 0 Z_{\odot}$, model u15, with $Z = 10^{-4} Z_{\odot}$, and model s15, with $Z = Z_{\odot}$. The initial perturbations are seeded by the grid. Calculations performed at twice the resolution in 2D indicate that our solutions are numerically converged. We find no significant difference in the width of the mixed region between our 3D and 2D simulations of the same supernova. Previous studies of Rayleigh-Taylor mixing in 1987A-type supernova models found that mixing was more efficient and individual Rayleigh-Taylor instabilities grew about 30% faster in 3D than in 2D. Kane et al. (2000) studied single-mode density perturbations with amplitudes of 10% of mode $l = 10$, and found that perturbations grew 30-35% faster in 3D than in 2D. The more recent study of Hammer et al. (2009) examined the post-explosion hydrodynamics of a 1987A-type model with a fully 3D explosion model from Scheck (2007) with large scale asymmetries at early times. They found that the instability grew about 30% faster in 3D than in 2D.

While we also find a faster initial growth rate in 3D than in 2D in our simulations, the growth rate in 3D declines once the simulations transition to turbulence, and the final width of the mixed region is the same in 2D and 3D. Because the Rayleigh-Taylor instability in our model is seeded by perturbations arising from the grid, our perturbations have a lower amplitude, and a flatter spectrum shifted towards higher modes than either the Kane et al. (2000) or Hammer et al. (2009) studies. In our progenitor models the Rayleigh-Taylor instability has more time to develop and grow than in previous simulations. With a growth time on the order of 10^5 seconds, instabilities in models s15 and z15 grow for more than 10 times longer than the simulations of Hammer et al. (2009), in which mixing froze out at around 9×10^3 seconds. In model u15, which died as a blue supergiant, mixing ceases after 4×10^4 seconds, which is a shorter time than the red giant models in this survey but is still nearly 5 times longer than the the simulations of Hammer et al. (2009).

In our progenitor models and with perturbations seeded by the grid the RT instability has enough time to grow that the fingers of the instability begin to interact with one another. This interaction transfers momentum and energy transverse to the shock, allowing the 3D simulations to mix more fully than 2D simulations. The more efficient transfer of momentum and energy in 3D renders the 3D simulations fully turbulent in the mixed region. This higher degree of mixing in 3D than in 2D reduces the Atwood number in the 3D simulations relative to the Atwood number in the 2D simulations. A lower Atwood number leads to a reduction in the bubble growth rate in 3D, which compensates for the lower

effective drag in 3D. The result is that the width of the mixed region is virtually identical between simulations performed in 2D and those performed in 3D. 3D simulations have transitioned to full turbulence and are more completely mixed than 2D simulations. This was found in a laboratory context in the simulations of Miles et al. (2005). For simulations in which interactions between the Rayleigh-Taylor fingers do not occur, either because only one finger is modeled (Anuchina et al. 2004) or the Rayleigh-Taylor fingers grow for a short enough time that they never interact (Kane et al. 2000), the greater effective drag experienced in 2D versus 3D will continue to dominate the simulation, ensuring that the width of the mixed region will be larger in 3D than in 2D. For simulations in which the Rayleigh-Taylor instability has enough time to grow that the fingers begin to interact with one another, the width of the mixed region will be the same in 2D and 3D simulations.

Instabilities arising from long wavelength perturbations take longer to grow than those arising from short wavelength perturbations. Large amplitude perturbations of long wavelength are necessary for such instabilities to grow substantially. These large-scale fingers may diverge before they can transition to turbulence, and thus may give rise to departures from axisymmetry. The large amplitude, long wavelength perturbations present in the more realistic explosion model of Hammer et al. (2009) ensure that such fingers don't interact, which results in the significant differences between their 2D and 3D simulations. Rayleigh-Taylor theory predicts that an inverse cascade, in which shorter wavelength instabilities merge to form longer wavelength instabilities, should be truncated long before the wavelength λ becomes comparable to the size of the region in which the instability is growing. Large scale departures from symmetry do not arise through an inverse cascade in our 3D simulations; they

must have their origins in the explosion itself.

It is likely that many, if not most, core-collapse supernovae explosions are highly asymmetric. Observations not just of 1987A but of other supernovae, as well as the "kicks" observed in pulsars, indicate that asymmetry is a near-universal phenomenon amongst the explosions of massive stars. From the theoretical side, it seems increasingly likely that viable supernovae explosions, like the SASI mechanism, are inherently asymmetric. In supernovae that die as red giants the Rayleigh-Taylor instability will have enough time to develop that individual fingers will interact with one another. If the asymmetries in such explosions are dominated by axisymmetric components, 2D models might well be good predictors of the width of the mixed region and the axisymmetric features of the remnant. Future work should investigate asymmetric explosions in a wide variety of progenitor models.

Work at UCSC and LBL was supported in part by the SciDAC Program under contract DE-FC02-06ER41438. Work at LANL was carried out under the auspices of the National Nuclear Security Administration of the U.S. Department of Energy at Los Alamos National Laboratory under Contract No. DE-AC52-06NA25396. Stan Woosley was supported by the NSF and NASA as well as SciDAC National Science Foundation (AST 0909129) and the NASA Theory Program (NNX09AK36G). The simulations were performed on the open cluster Coyote at Los Alamos National Laboratory. Additional computing resources were provided on the Pleiades computer at UCSC under NSF Major Research Instrumentation award number AST-0521566. C.C.J. would like to thank Andrew Aspden for assistance with parallelizing a data reduction routine. Figure 5 was created using VisIt.

REFERENCES

- Almgren, A. S., Bell, J. B., C., J., S., D. M., H., H. L., M., S., & M., Z. 2010, /apj
- Anuchina, N. N., Volkov, V. I., Gordeychuk, V. A., Es'kov, N. S., Ilyutina, O. S., & Kozyrev, O. M. 2004, *J. Comput. Appl. Math.*, 168, 11
- Arnett, D., Fryxell, B., & Mueller, E. 1989, *ApJ*, 341, L63
- Blondin, J. M. & Mezzacappa, A. 2006, *ApJ*, 642, 401
- Blondin, J. M., Mezzacappa, A., & DeMarino, C. 2003, *ApJ*, 584, 971
- Burrows, A., Dessart, L., Livne, E., Ott, C. D., & Murphy, J. 2007, *ApJ*, 664, 416
- Burrows, A., Livne, E., Dessart, L., Ott, C. D., & Murphy, J. 2006, *ApJ*, 640, 878
- Chevalier, R. A. 1976, *ApJ*, 207, 872
- Chugai, N. N. 2006, *Astronomy Letters*, 32, 739
- Chugai, N. N., Fabrika, S. N., Sholukhova, O. N., Goranskij, V. P., Abolmasov, P. K., & Vlasyuk, V. V. 2005, *Astronomy Letters*, 31, 792
- Ekström, S., Meynet, G., Chiappini, C., Hirschi, R., & Maeder, A. 2008, *A&A*, 489, 685
- Fryxell, B., Arnett, D., & Mueller, E. 1991, *ApJ*, 367, 619
- Hachisu, I., Matsuda, T., Nomoto, K., & Shigeyama, T. 1990, *ApJ*, 358, L57
- . 1992, *ApJ*, 390, 230
- Hammer, N. J., Janka, H., & Mueller, E. 2009, *ArXiv e-prints*
- Hanuschik, R. W., Thimm, G., & Dachs, J. 1988, *MNRAS*, 234, 41P
- Herant, M. & Benz, W. 1991, *ApJ*, 370, L81
- . 1992, *ApJ*, 387, 294
- Herant, M. & Woosley, S. E. 1994, *ApJ*, 425, 814
- Hirschi, R. 2007, *A&A*, 461, 571
- Janka, H., Langanke, K., Marek, A., Martínez-Pinedo, G., & Müller, B. 2007, *Phys. Rep.*, 442, 38
- Joggerst, C. C., Almgren, A., Bell, J., Heger, A., Whalen, D., & Woosley, S. E. 2010, *ApJ*, 709, 11
- Joggerst, C. C., Woosley, S. E., & Heger, A. 2009, *ApJ*, 693, 1780
- Kane, J., Arnett, D., Remington, B. A., & Glendinning, S. G. 2000, *ApJ*, 528, 989
- Kifonidis, K., Plewa, T., Janka, H.-T., & Müller, E. 2003, *A&A*, 408, 621
- Kifonidis, K., Plewa, T., Scheck, L., Janka, H.-T., & Müller, E. 2006, *A&A*, 453, 661
- Löhner, R. 1987, *Comput. Methods Appl. Mech. Eng.*, 61, 323
- Marek, A. & Janka, H.-T. 2009, *ApJ*, 694, 664
- Matz, S. M., Share, G. H., Leising, M. D., Chupp, E. L., & Vestrand, W. T. 1988, *Nature*, 331, 416
- Miles, A. R., Blue, B., Edwards, M. J., Greenough, J. A., Hansen, J. F., Robey, H. F., Drake, R. P., Kuran, C., & Leibbrandt, D. R. 2005, *Physics of Plasmas*, 12, 056317
- Mueller, E., Fryxell, B., & Arnett, D. 1991, *A&A*, 251, 505
- Rayleigh, L. 1883, *Proceedings of the London Mathematical Society*, 14, 170
- Remington, B. A., Drake, R. P., & Ryutov, D. D. 2006, *Reviews of Modern Physics*, 78, 755
- Scheck, L. 2007, PhD thesis, Technical University, Munich
- Scheck, L., Kifonidis, K., Janka, H.-T., & Müller, E. 2006, *A&A*, 457, 963
- Utrobin, V. P. 2004, *Astronomy Letters*, 30, 293
- Wang, L. & Wheeler, J. C. 2008, *ARA&A*, 46, 433
- Woosley, S. E. & Heger, A. 2007, *Phys. Rep.*, 442, 269
- Zhang, W., Woosley, S. E., & Heger, A. 2008, *ApJ*, 679, 639